NAIC-ID(RS)T-0512-95

NATIONAL AIR INTELLIGENCE CENTER

THERMAL BLOOMING OF LASER PULSES, SPECKLE FIELD IN TURBULENT ATMOSPHERE, WAVEFRONT SENSOR, AND OPTICAL UNSTABLE RESONATORS
(Selected Articles)

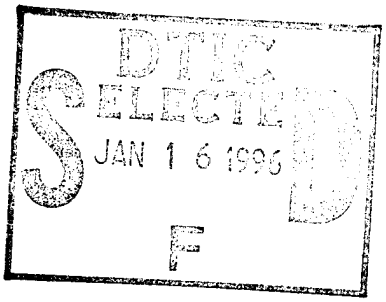

Approved for public release: distribution unlimited

HUMAN TRANSLATION

NAIC-ID(RS)T-0512-95 8 December 1995

MICROFICHE NR: 95C0000758

THERMAL BLOOMING OF LASER PULSES, SPECKLE FIELD IN TURBULENT ATMOSPHERE, WAVEFRONT SENSOR, AND OPTICAL UNSTABLE RESONATORS (Selected Articles)

English pages: 60

Source: Qiangjiguang Yu Zizishu (High Power Laser and Particle Beams), Vol. 5, Nr. 3, August 1993; pp. 394-404; 445-448; 469-480.

Country of origin: China
Translated by: Leo Kanner Associates
F33657-88-D-2188
Requester: NAIC/TATD/Bruce Armstrong
Approved for public release: distribution unlimited.

TABLE OF CONTENTS

GRAPHICS DISCLAIMER

All figures, graphics, tables, equations, etc. merged into this translation were extracted from the best quality copy available.

WHOLE-BEAM THERMAL BLOOMING EXPERIMENTS WITH LONG LASER PULSES

Liu Changling, Hu Xijing, Yuan Yonghua.
Gui Yuanzhen, Zhang Kexing, Li Qiming,
Wang Chunyan, Liu Xufa, and Yang Libing

Southwest Institute of Fluid Physics
P.O. Box 523, Chengdu 610003

ABSTRACT Whole-beam thermal blooming experiments have been done using a focused long pulse laser (τ_p=1.8ms, E=200J, angle spread θ=2mrad). A blooming cell is full of ammonia at 0~6 atmosphere pressure. A CCD system is used to measure the diameter of the distorted laser beam waist and the intensity profile of the spot at waist. The absorption cofficients are measured by a digital calorimeter. The instantaneous irradiation intensity at spot centre is measured by a photodiode digital collector-Roland mapper-Computer system. The instantaneous intensity profile is measured by a high speed camera.

KEY WORDS absorption, blooming, distortion, laser atmosphere propagation.

I. Introduction

The reason for paying attention to the transmission of high-powered lasers in the atmosphere is mainly because these can become a new-generation strategic weapon. One of the main approaches in attacking targets in space is to induce structural failure of the target with the thermal and mechanical effects of the laser. High-powered laser systems are required to produce such destruction. Therefore the authors are studying the nonlinear effects of high-powered lasers in atmospheric

transmission; there is practical significance such as absorption, scattering, atmospheric turbulence, thermal blooming, gas puncturing, excited Raman scattering, and optical compensation.

The effect of thermal blooming is due to absorption of laser energy in the laser beam by the atmosphere so that the initial medium in thermal equilibrium is heated locally to cause an increase in gas density and raise the speed of sound, thus inducing changes in refractivity and causing a negative-lens effect to scatter the laser beam. Thus, the light beam dimensions are increased at the focal plane to cause light-spot anomalies. For systematic research, frequently some absorptive media are used to simulate atmospheric absorption for thermal blooming research in laboratories. There are different kinds of thermal blooming with different laser acting periods. When classified by time properties, there are continuous-wave lasers, pulsed lasers, and repetition-frequency pulsed lasers. There are two thermal blooming situations for single-pulse lasers. Which situation is involved is determined by the time (of flow dynamic properties) $\tau_H=D/c_s$. D is the light beam diameter; c_s is the speed of sound in the medium; and τ_H is the time required for sound wave to pass through the light beam cross-section in the absorbing medium. When the laser pulse time $t_p<\tau_H$, the density disturbances in the laser beam increases as the third power of time; this is called the tertiary thermal blooming effect. When $t_p>t_H$, the density disturbances increase in proportion to time. In this experiment, what decided by the light-beam diameter,

$\tau_H << t_p$ is the first-power of the thermal blooming effect.

Detailed experimental and theoretical studies were conducted between the thermal blooming effect and time in the transmission of high power lasers that were carried out abroad. In [1,2], a CO_2 laser operating at 10.6micrometers was used. In references [3,4], measurements of the time process of a 1.06micrometer neodymium glass laser were carried out, thus yielding the relatively consistent results compared with the theoretical estimates. In 1973, at Lincoln Laboratories [4] in the United States, the 1.06micrometer pulsed laser (E_p=20 to 200J, β=50), NH_3 of 0.6MPa was used as the absorbing medium to simulate absorption in the atmosphere. Experiments on the time process of various laser pulses were conducted. In the authors' experiments, thermal blooming experiments and research were conducted by using 1.8ms of pulse time, 200J of output energy, in the free-oscillation neodymium glass laser of light-beam divergence angle of 2mrad (β=20), in free oscillations with lens focusing while passing a thermal blooming cell filled with ammonia at 0 to 0.6MPa. A CCD system was used to measure the variational curve between the time-integrated light meter and the ammonia pressure of the thermal blooming cell of the laser beam waist. With an energy meter that had a digital display and peak value retention, the absorption coefficient was measured after the laser beam had passed through the ammonia cell. A complex of silicon optoelectronic diode/digital collection and analysis instrument/Roland automatic plotter/computer processing system

was used to determine the time-dependent variation curve and light-intensity-gas pressure in ammonia cell-time curve, for the central light intensity of the laser.

By using the KDP frequency doubler/high-frequency frame dividing camera system to record the light intensity distribution-time image after the laser beam had passed through the ammonia cell, thus we obtained frame-by-frame photographs, and observation of the time-dependent anomaly of the light-beam field intensity. Thus, beam broadening and central hollowing phenomenon (the intensity in the light beam center decreased, and the intensity at the beam periphery was greater than the center intensity), after the light spot had passed through the thermal blooming cell. The experimental results are basically in agreement with theory.

II. Brief Description of Analytical Theory [5]

Based on the conservation of energy, in the approximate conditions of the side axis, the light intensity I satisfies the following equation:

$$\int \nabla_r n dz \nabla_r I + \int \nabla_r n dz \nabla_r I + \frac{I}{n} \int \nabla_r^2 n dz = -\alpha I \qquad (1)$$

In the equation, n indicates the refractivity of the medium; r indicates the horizontal direction; and ρ indicates the total absorption coefficient of the medium.

Under the conditions of neglecting the longitudinal-gradient of the refractive index, neglecting the diffraction effects,

(that is, the application of geometric optics), Eq. (1) can be written in integrated form

$$\frac{I(r,z)}{I(r,0)} = \exp\{-\alpha z - \int_0^z (\nabla_r - \nabla_r I / I) \int_0^{z'} \frac{\nabla_r n}{n_0} dz'' dz'\} \qquad (2)$$

The variations of the refractive index n and density ρ of the gas with time satisfies the Dale-Gladesrone law:

$$n - 1 = \kappa \rho \qquad (3)$$

In the equation, κ is the proportional constant.

In the transmission problem of single-pulse lasers, it is required to consider the variation of density with time. Based on the equation sets in fluid mechanics, the density ρ satisfies

$$(\frac{\partial^2}{\partial t^2} - c_s^2 \nabla^2) \frac{\partial \rho}{\partial t} = (\gamma - 1) \alpha \nabla^2 I \qquad (4)$$

In the equation, c_s is the speed of sound in the absorbing medium; $c_s^2 = \gamma p / \rho$, $\gamma = c_p / c_v$, c_v is the ratio of specific heat; and ρ is the gas pressure of the absorbing medium.

The equation for the ideal state of the gas is

$$p = \rho R T \quad , \quad R = c_p (1 - \frac{1}{\gamma}) \qquad (5)$$

The problems being studied by the authors include the fact that the first term $t_p > t_H$ in Eq. (4) can be neglected. By integrating Eq. (4) with respect to time, we have

$$\rho - \rho_0 = -\int_0^t \frac{\gamma - 1}{c_s^2} \alpha I dt = -\frac{\gamma - 1}{c_s^2} \alpha \int_0^t I dt = -\frac{\gamma - 1}{c_s^2} \alpha \frac{1}{\pi a^2} \int_0^t P(t) dt \qquad (6)$$

If a laser beam is a rectangular pulse, then Eq. (6) is

$$\rho - \rho_0 = -\frac{\gamma - 1}{c_s^2} \alpha \frac{1}{\pi a^2} P(t) \qquad (7)$$

With respect to a gaussian light beam, from Eqs. (2), (3), (5), and (6), we can obtain the analytical solution for light-intensity distribution after passing through the absorbing medium:

$$\frac{I(r,z,t)}{I(r,0,t)} = e^{-\alpha z}\exp\left\{\frac{2n_T\alpha\int_0^t P(t)dtz^2}{\pi n_0\rho c_p a^4}\, g(az)e^{-\frac{r^2}{a^2}}\left(1-\frac{2r^2}{a^2}\right)\right\} \tag{8}$$

In the equation

$$g(\alpha z) = \frac{2}{\alpha z}\left[1-\frac{1}{\alpha z}\left(1-e^{-\alpha z}\right)\right] \tag{9}$$

The anomaly parameter of defining the alignment beam

$$N_c = -\frac{2n_T\alpha\int_0^t P(t)dtz^2}{\pi n_0\rho c_p a^4}\, g(\alpha z) \tag{10}$$

Eq. (8) is transformed to become

$$\frac{I(r,z,t)}{I(r,0,t)} = e^{-\alpha z}\exp\left\{-N_c e^{-\frac{r^2}{a^2}}\left(1-\frac{2r^2}{a^2}\right)\right\} \tag{11}$$

In Eq. (10), n_T is dn/dT; this is a negative value for n_T of most gases, and ρ is the absorption coefficient, P(t) is the laser power of the laser device; z is the length of the absorbing medium; n_0 is the refractive index of the gas without disturbances; ρ_0 is the initial density of the absorbing medium; c_p is the isobaric specific heat. ρ is the beam radius when the light intensity is reduced to 1/e.

In Eq. (11), I(r,0,t) is the intensity distribution of the laser beam without thermal blooming. For a gaussian light beam, we have

$$I(r,0,t) = I_0(t)e^{-\frac{r^2}{a^2}} = \frac{P_0(t)}{\pi a^2}\, e^{-\frac{r^2}{a^2}} \tag{12}$$

In the equation, $P_0(t)$ is the initial power of the laser beam. Eq. (11) is the theoretical result of the medium with respect to the straightening situation. This should be revised for a focusing beam. Assume that the focusing beam satisfies the geometric-optics approximation, in other words,

$$\frac{a_z}{a_0} = 1 - (1 - \frac{a_f}{a_0}) \frac{z}{z_f} \tag{13}$$

Refer to Fig. 1 for the light-path diagram. In the equation, a_0 is the light beam initial radius, a_f is the radius of the focal spot; z_f is the focal distance; and a_z is the beam radius at distance z.

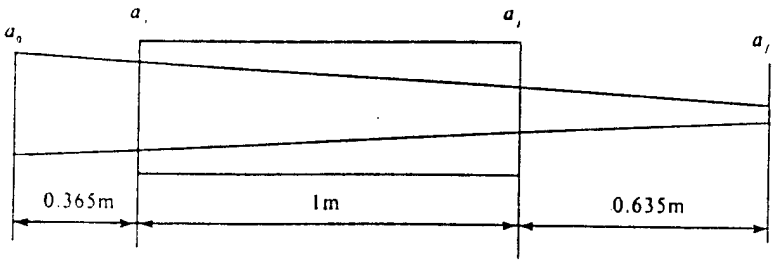

Fig. 1 Arrangment of blooming cell

For long pulses ($t_p > \tau_H$)

$$N_e = N_c q (\frac{a_i}{a_f}) \tag{14}$$

$$q(x)=\frac{x^2-1-2\ln x}{2(1-\frac{1}{x})^2}\ ,\ x=\frac{a_i}{a_j} \tag{15}$$

When x=1, q=1. When x>>1, q(x) is proportional to $x_2/2$.

In Eq. (13), a_i is the beam radius at z=0. a_j is the beam radius at z=L (exit of blooming cell).

The temperature rise generated by the medium when absorbing laser energy is

$$\Delta T=\frac{\alpha E}{\rho c_p S} \tag{16}$$

In the equation, the unit of α is m^{-1}; E(J) is the pulse energy; and S (m^2) is the cross-sectional area of the light beam. The rate and time of thermal expansion [5] are

$$v_T=\frac{\kappa}{\rho c_p a}\ ,\quad \tau_T=\frac{D}{v_T} \tag{17}$$

κ ($W\cdot m^{-1}\cdot K^{-1}$) is the coefficient of thermal expansion. The convection rate and the property time induced by the floating force are given by

$$v_{NC}=(\frac{2\alpha Pg}{\rho c_p T})^{1/3}\ ,\quad \tau_B=\frac{D}{v_{NC}} \tag{18}$$

In the equation, g is acceleration due to gravity and D is the beam diameter.

The characteristic time in fluid mechanics is given by

$$\tau_H=\frac{D}{c_s} \tag{19}$$

From Eq. (13) we obtain: $a_i=0.867\text{cm}\ ,\ a_j=0.502\text{cm}.$

From Eq. (15), the correction factor (of the focusing beam) q(x)=2.508.

III. Whole Beam Thermal Blooming Experimental System of a Long-Pulse High-Powered Laser

From Fig. 2, the overall layout of the experimental system, we can see that a free-oscillating neodymium glass laser device

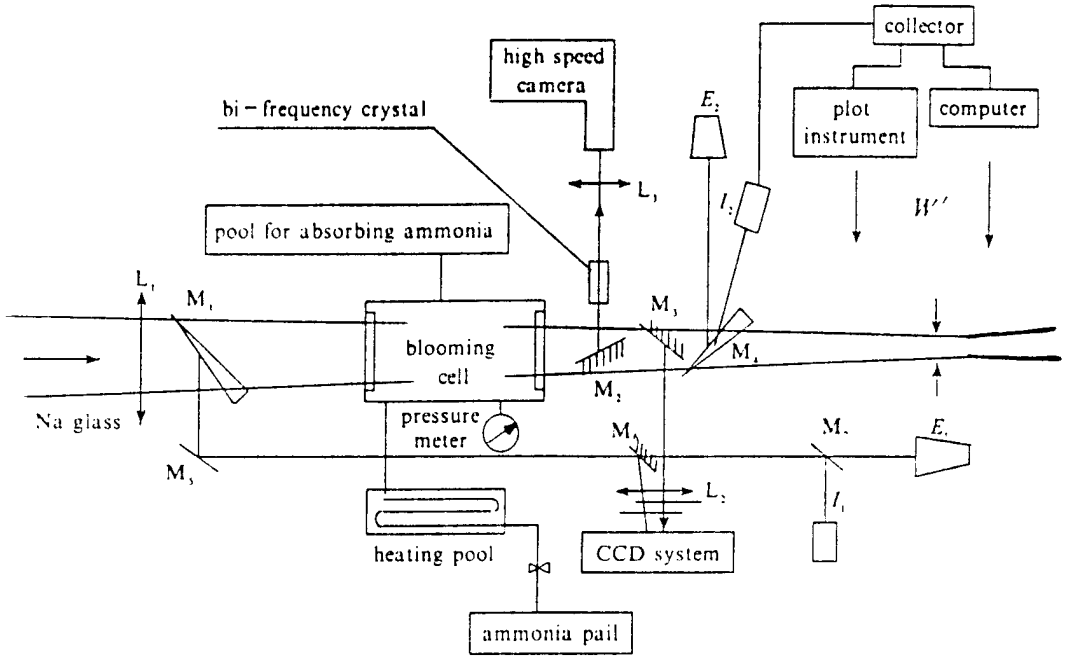

Fig. 2 Whole-beam blooming experimental layout

with 200J output energy and 1.8ms pulse time is used in order to carry out the experimental research on whole-beam thermal blooming and in obtaining the required parameters of the thermal-blooming effect. A blooming cell with ammonia at the highest pressure 0.6MPa was used with the optimal beam diameter at OD20mm and optical beam divergence angle of 2mrad for the output of a parallel plane cavity. The blooming cell consists of an OD0.1mx1m stainless steel tube flange system, valve, and pressure gauge for measuring the ammonia gas pressure in the cell. Both ends of the tube are sealed with optical windows of high optical quality. The ammonia gas in the cell is used to simulate the

laser of the absorbing medium of the atmosphere. This arrangement is used to focus the high-powered laser beam after focusing and passing through the 2m focal length of the blooming cell to focus onto the convergent lens L_1 and other transmission and reflective optical components.

With respect to the test system after the focusing light beam passes through the light cell, the test system is used for the variation of ammonia pressure in the blooming cell with the time-integrated diagram of the laser beam waist. The absorption coefficient test system for variation in ammonia pressure after the focused laser beam has passed through the blooming cell. The following four components constitute a controlled system synchronized with the experiment: the central intensity of the laser, with dependence on the laser pulse, measurement processing system varying with ammonia gas pressure, distribution of field intensity of the laser beam cross-section after passing through the blooming cell, and the test system for development variation of anomalies with time. After the laser is focused through the convergent lens and passes through the blooming cell, when there is no ammonia in the cell, the output of the light spots with relatively concentrated field intensity is shown with photographic paper recording the laser beam waist (Fig. 3). When the cell is filled with 0.1 to 0.6MPa ammonia gas from low to high, these light spots gradually diverge, decay, and are

anomalous with respect to pressure intensity (Figs. 3b, c, d, e, f, g).

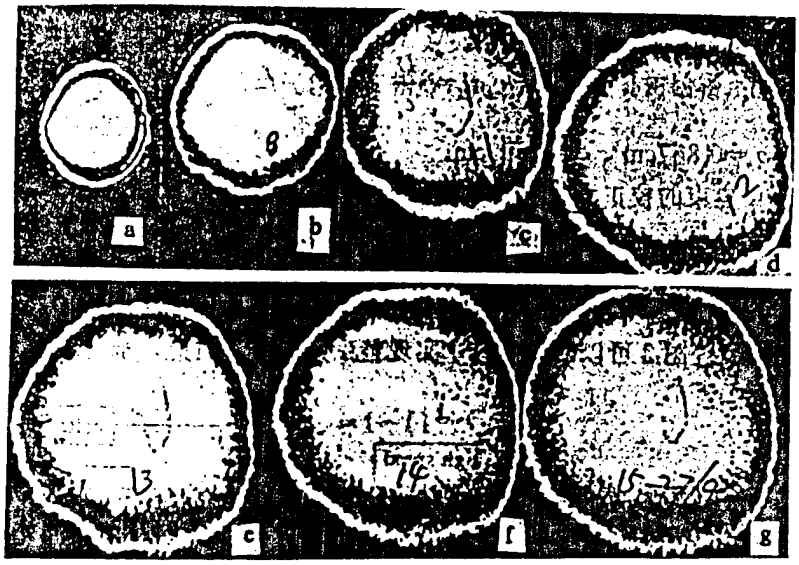

Fig. 3 Spots of laser waist on photographic printing paper for 0 ~ 0.6MPa ammonia pressure in the blooming cell

IV. Experimental Tests and Analysis of Thermal Blooming Effects

4.1. Time-integrated Image of Focused Laser Beam Waist

As shown in Fig. 1, after reflection with convergence through lens L_1, the 200J pulsed laser beam passes through an optical wedge M_1 with single-plane reflectivity of 4%, reflective mirrors M_5 (R=95%), and M_6 (R=95%), the beam waist of the light beam falls onto an unfinished glass screen in front of the optical lens of the CCD camera. This laser beam does not pass through the blooming cell. The portion of the laser beam passing through the optical wedge M_1 and after passing through a blooming cell filled with ammonia gas at a different pressure and

reflected through optical wedge M_3 (R=4%), the beam waist of this laser beam also is incident on the unfinished glass. The light intensity distribution diagram of both laser beam waists are integrated on the CCD during the entire time period of 1.8ms, and is collected and processed with a computer connected to the CCD camera. Thus, on the computer screen the color two- and three-dimensional field-intensity distribution diagrams of time integration of two laser beam waists, one passing through, and the other not passing through the blooming cell; the diameters of the two laser beam waists are shown. In Fig. 4a and b are shown

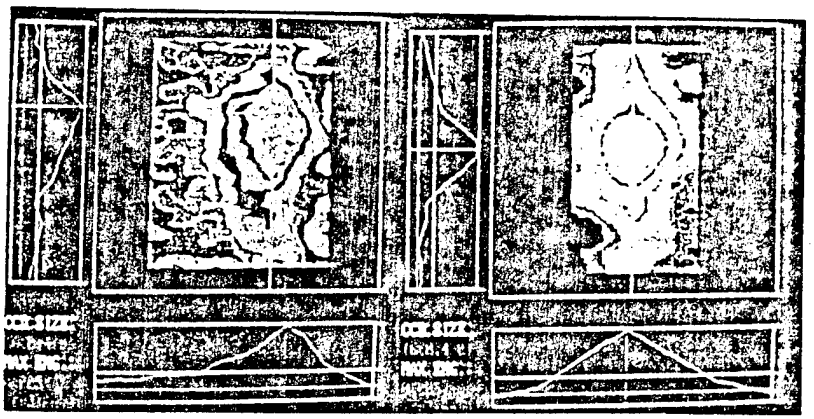

(a) (b)

Fig. 4 Time-intergrated 2D intensity at beam waist measured by CCD system

two-dimensional color light intensity distribution diagrams and the derived data of beam waist diameters for the laser beam waist of the blooming cell filled with 0.1 to 0.5MPa ammonia. When the blooming cell is filled with 0 to 0.6MPa ammonia, respectively, then the field intensity distribution diagrams of seven beam

waists and diameter data for the beam waist are obtained as shown in Fig. 5 and Table 1.

Table 1 Diameterd at beam waist

表 1 束腰直径数据

p 0.1MPa	0	1	2	3	4	5	6
d mm	4	4.28	4.51	6.88	8.83	9.83	13

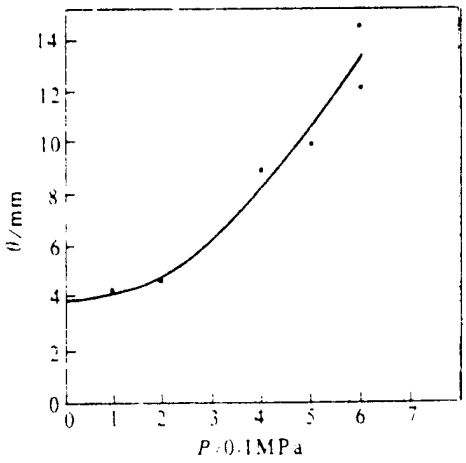

Fig. 5 Curve of diameter at beam waist versus ammonia pressure

4.2. Laser Beam Absorption Coefficient When Beam Passes Through Blooming Cell

From Fig. 2 the laser beam not passing through the blooming cell is reflected by M_1 and M_5, and then passes through M_6 (T=0.05) and M_8 (T=0.92) to arrive at the energy meter E_1. The other laser beam passes through the front window opening (T=0.92) of the blooming cell and M_1 (T=0.92), then passes through the blooming cell before passing through the rear window opening of

the blooming cell, wedge lengths M_2 and M_1 (T=0.92), and then reflected (R=0.04) from the front surface of the wedge length M_4 to arrive at the energy meters E_2 and E_1. Records of the energy recording instruments are stored as digital peak values with E_2. Laser energy E_1 not passing through the blooming cell, and E_1 passing through the blooming cell are measured, respectively. Since both light beams pass through different optical systems, it is required to divide with the transmission coefficients the measured energy E_1 and E_2 of both energy meters to obtain the actual energy. Since there are system errors in the two energy meter systems, it is required to calibrate (in order to remove system errors) of the two energy test systems before the blooming cell is filled with ammonia and in the condition of laser device output of a certain amount of energy. The blooming cells are filled, respectively, with ammonia gas at 0 to 0.6MPa. Under the conditions of 200J energy outputted from the laser device, the absorption coefficients (Table 2) are obtained for passage

Table 2 Absorbtion coefficients in blooming cell

p/MPa	0	0.1	0.2	0.3	0.4	0.5	0.6
α/m^{-1}	0.0054	0.076	0.21	0.54	0.68	0.88	1.06

through the 1m blooming cell. Thus, the curve of the absorption coefficients was obtained for a laser by the ammonia blooming cell of 0 to 0.6MPa (Fig. 6).

4.3. Time Variation Curve of Central Light Intensity of Laser Beam

The time variations of laser pulses versus central light intensity (Fig. 7) of the laser after passing through the 0 to 0.6MPa ammonia blooming cell are recorded, respectively, with a silicon light-emitting diode/digital collection and analysis

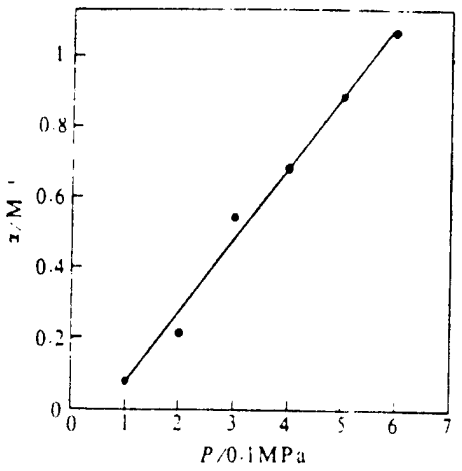

Fig. 6 Curve of absorption colficient versus ammonia pressure

instrument/automatic plotter (Fig. 2). From the wave curves of these six lasers we can see that absorption is higher for a laser beam passing through a cell with higher ammonia gas pressure. After the laser beam passes through the blooming cell filled with 0.3MPa gas, the central light intensity of the laser of 1.8ms laser pulse time has its peak intensity reduced to approximately 1.3 at the time of 400microseconds. After 1.2ms, the intensity drops to almost zero. When passing through the blooming cell

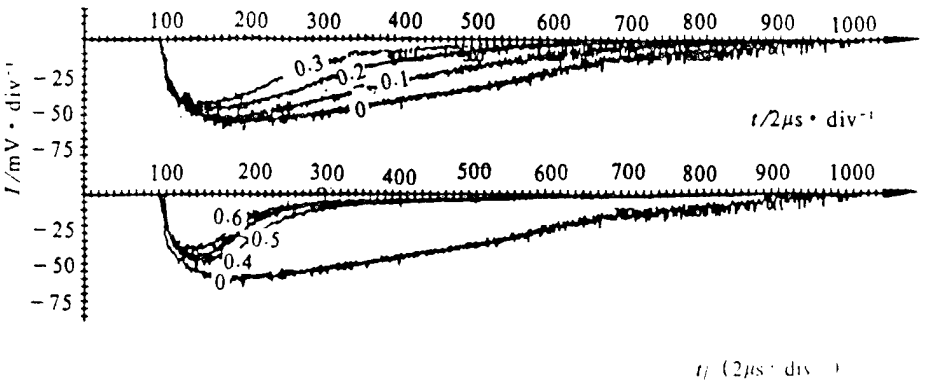

Fig. 7 Curve of intensity at the centre versus time, the values across curves indicate atmosphere pressure inside blooming cell

filled with ammonia at a gas pressure of 0.6MPa, the central light intensity of the laser beam drops to one-third of the peak value intensity only after 200microseconds. After 1ms, it drops to almost zero. The light intensity curve I and time t of the central time intensity curves of the six light beams are processed with a computer system to compare with the light intensity I_0 of the blooming cell with ammonia gas dropping to 0 as the light beam passes through, the time versus variation curve of the laser pulse with the central light intensity of the laser can be obtained (Fig. 8).

4.4. Anomalous Images of Light Intensity Distribution of Laser Beam

When a laser beam passes through a blooming cell filled with ammonia gas, as the effect of thermal blooming induces the absorbing medium in the optical path to generate a negative-lens

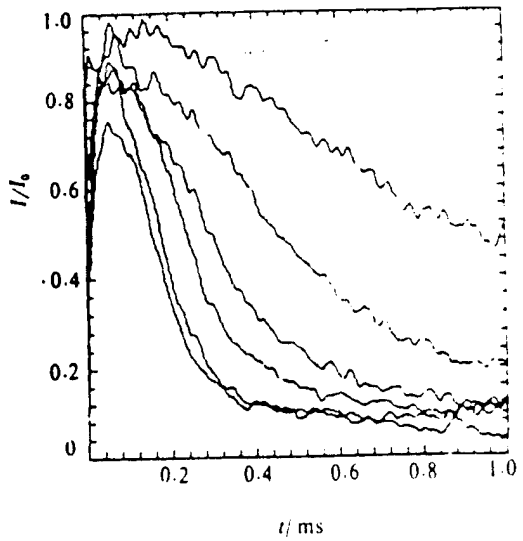

Fig. 8 Curve of I/I_0 at the centre versus time

effect, the light intensity of the laser beam continuously increases with development anomaly of the laser pulse type. To obtain the real-time image of the anomaly, a high-speed frame-by-frame camera of 25,000 frames per second is used to record the images. Since the laser wavelength outputted from the neodymium glass laser device is 1.06micrometers, light exposure is not obtained for the conventional high-speed photographic negative. Therefore, the authors used the KDP crystal frequency doubler. By using a neodymium glass laser device with pulse time 1.8milliseconds, when the 200J laser energy arrives at the KDP crystal frequency doubler by passing through the optical path as shown in Fig. 1, the light intensity distribution outputted with doubled frequency is measured with a CCD light intensity analysis system. As indicated in the results, the light intensity

distribution is proportional to the light intensity distribution prior to frequency doubling. Fig. 9 shows the high-speed frame-

Fig. 9 The instantanous irradiation instensity of the spot at different time (the duration between two spots in succession is 40μs)

by-frame pictures with field intensity distribution of the laser beam after the laser beam passes through the thermal blooming cell filled with ammonia gas at a pressure of 0.6MPa. From these frame-by-frame pictures, there is only 40microseconds from the second frame to the third frame, great anomaly is generated in field intensity distribution, thus a large empty area appeared in the central light intensity of the light beam. Hereafter, the light beam rapidly diverges, and the empty hole quickly expands, leading to lower and lower local light intensities in the two-dimensional distribution of the light beam.

V. Discussion of Experimental Results

Tables 3 and 4 show the parameters of ammonia gas and laser beams used in the experiment. In the tables, K is the thermal conductivity coefficient, and D is the initial diameter of the laser beam. Based on Eq. (14) and the absorption coefficient

Table 3 NH_3 parameter in experiment

ρ_0/(kg·m^{-3})	n_T	n_0	c_p/(kJ·kg^{-1}·K^{-1})	c_s/(m·s^{-1})	K/(W·m^{-1}·K^{-1})
0.759	1.283×10^{-3}	1.000376	2.241	415	0.21

Table 4 Parameter laser set

E/J	t/ms	λ/μm	D/mm	θ/mrad	β
200	1.8	1.06	20	2	20

α measured in the experiment, the anomaly parameter N_c and the temperature rise of ammonia at different pressures are listed in Table 5. From Table 5, when the ammonia gas pressure is higher than 0.1MPa, N_e>10, and Δ>10%. Therefore, the analytical theory is not applicable here.

Table 5 Distortion parameter N_c and risen temperature ΔT versus ammonia pressure

P/0.1MPa	0	1	2	3	4	5	6
N_c	0.93	12.7	34.2	78.4	94.6	115.5	132.2
T/K	17.8	225	421	802	807	871	899

With the estimate from analytical theory and the experimental results of the central light intensity of laser beams, due to limitations of the analytical theory, the authors can discuss only one situation, that the ammonia gas pressure is

0. Fig. 10 indicates the time spectrum of laser intensity at the

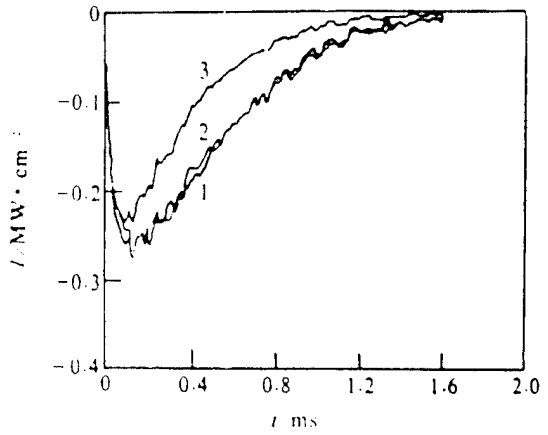

Fig. 10 Irradiation intensity at the centre of its waist versus time after light beam goes through a cell with 0 pressure
1. laser source; 2. experimental result; 3. analytical theory result

light beam center. This indicates that the theoretical curve and the experimental curve are in agreement with each other. For comparison, similar curves (Fig. 11) are also given for the blooming cell at a gas pressure of 0.1MPa. Here, the anomaly parameter has attained a value of about 10. From Fig. 11, the difference between theoretical and experimental values are relatively high.

With respect to the theoretical and experimental values of time integration of the laser beam waist diameters, based on the analytical theory in the second section, time integration is conducted on the point r=0 in Eq. (8), the time integration values on light beam central intensity are calculated, respectively, in order to compare with the central intensities of

time integration measured with the CCD.

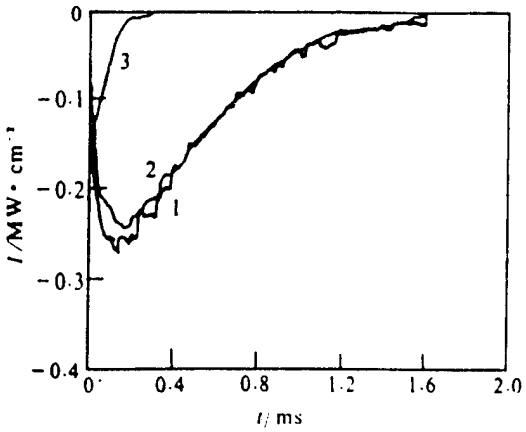

Fig. 11 Irradiation intensity at the centre of its waist versus time after light beam goes through a cell with one pressure
1. laser source; 2. experimental result;
3. analytical theory result

The value of time integration for light beam central intensity is I_0. After passing through the absorption cell with ammonia gas pressure at 0MPa, the time integration value of the light beam central intensity is I_1, then the theoretical value I_1/I_0 is 0.44 and the corresponding experimental value is 0.63. We can see that the theoretical and experimental values are in relative agreement with each other.

VI. Conclusions

(1) The whole-beam thermal blooming experiment with long pulses was successful. The absorption coefficient of ammonia gas for a light beam of 1.06micrometer wavelength was measured. The

beam broadening and anomaly phenomena of the laser beam due to the effect of thermal blooming was observed.

(2) The analytical theory of whole-beam thermal blooming can be adaptable only to weak anomalies. When the anomaly parameter is approximately over 10, the numerical simulation calculation of nonlinear optics should be applied in order to precisely describe the thermal blooming phenomenon. Based on the authors' experimental data, the numerical simulation calculations were conducted by Li Youkuan of the Beijing Institute of Applied Physics and Computational Mathematics, obtaining six curves (Fig. 12) showing the time variation of central light intensities

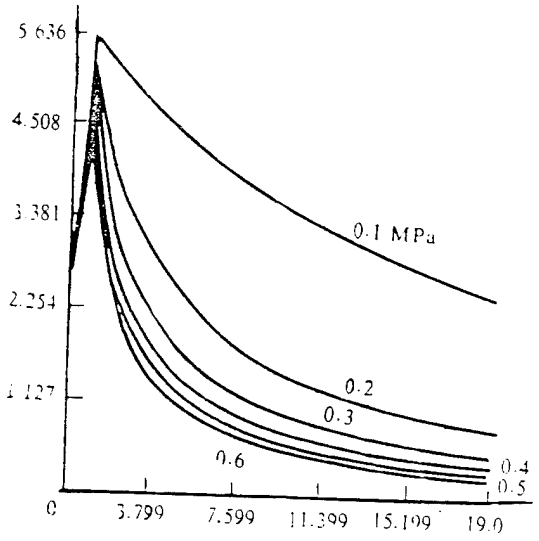

Fig. 12 Curve of intensity at the centre versus time

of lasers passing through a blooming cell containing ammonia gas at a pressure of 0.1 to 0.6MPa. The abscissa in the figure shows 19 equal divisions when the maximum pulse time value is 1ms. The vertical axis is the dimensionless value of I/I_0 of the laser

central light intensities. The unified value of 5.636 is 1. The time-dependent anomaly of three-dimensional field intensity distribution of laser beams when the ammonia gas pressure is 0.3MPa was also obtained (in Fig. 13, the time gap between each of four frames of figures is 0.3ms). From the comparison of the

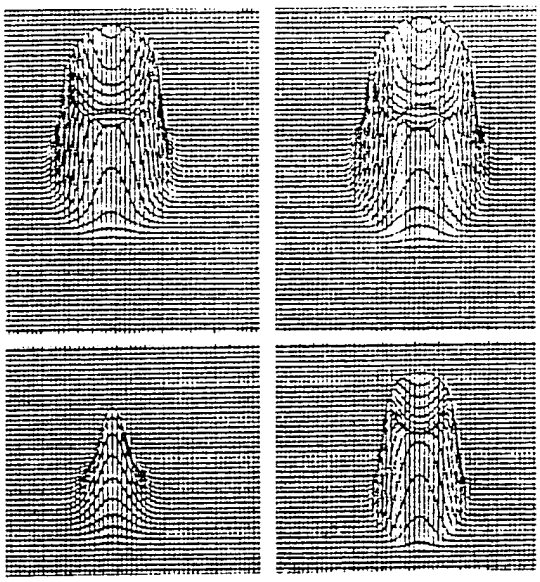

Fig. 13 3D intensity of laser beam versus time

numerical simulation calculation results and the thermal blooming experimental results, there is a relatively good consistency.

(3) From the results of testing the absorption coefficients in Table 2, when the laser energy is about 200J, the absorption coefficient is $0.076M^{-1}$ when the gas pressure in the blooming cell is 0.1MPa. As indicated by repeated experiments, the data obtained by the authors are reliable.

The first draft was received on February 9, 1993; the final revised draft was received for publication on May 6, 1993.

REFERENCES

[1] Kenemuth JR, Hogge CB and Avizonis PV, *Appl Phys Lett*, 1970, **17** (5): 220.

[2] Buser RG and Rohde RS, *Appl Opt*, 1975, **14** (1): 50.

[3] Longaker PR and Litvak MM, *J Appl Phys*, 1969, **40** (10): 4033.

[4] Leiman HK and Oneil RW, *Appl Phys Lett*, 1973, **23** (1): 43.

[5] David CS, *Proc IEEE*, 1977, **65** (12): 1679.

UNWRAPPED-PHASE DISTRIBUTION OF A SPECKLE FIELD IN TURBULENT ATMOSPHERE

Zhang Yixin, Department of Mechanics,
Wuxi College of Light Industry, Wuxi 214036
Chi Zeying and Chen Wenjian, Department of
Photoelectrical Engineering, East China College
of Technology, Nanjing 210014

ABSTRACT Based on the statistic independent property of the effects of rough surface and atmospheric turbutence on a propagation laser beam, a formulation for the probability density function of the unwrapped phase of a elliptic Gaussian speckle field that propagates through clear air turbulence is developed.

KEY WORDS unwrapped phase, probability density function, turbulent atmosphere.

I. Introduction

Multiple modes [1-3] have been proposed for speckle fields formed by scattering of diffusing light beam particles, and phase probability density function of a light passing through clear atmospheric turbulence. These models describe the probability distribution of the wrapped phase fluctuations of radian values between 0 and 2π for the phase variation. However, in practical applications of adaptive compensation and precise ranging, we often confront a situation in which the phase fluctuations of

optical waves often exceeds 2Π radians. Therefore, a study of the distribution rule that unwrapped phase varies with surface height fluctuations and eddy current intensity when exceeding 2Π radians for the phase fluctuations of light waves is a more important and practical problem. This problem was recently analyzed by Draper [4]; however, Draper et al. neglected the noncircularity of the unsmooth and scattered echo waves. We know from studying the statistical distribution theory and experiments subject to speckle fields of scattered echo waves from unsmooth boundary surfaces that a more objective distribution of the speckle field of scattered echoes from unsmooth surfaces should be elliptical gaussian distribution [5], therefore the ellipticity parameter will be introduced in the paper to analyze the oscillation amplitude of the scattered echo wave field of the positioning target, which can satisfy the unwrapped phase probability distribution after speckles (of elliptic gaussian distribution) pass through the atmospheric turbulence.

II. Theoretical Analysis

Since the random fluctuations of the target boundary surface and fluctuations of atmospheric turbulence are interdependent, the atmospheric turbulence and the target (unsmooth surface) independently lead to phase fluctuations of optical waves. In analysis, the authors consider the interference between target and atmospheric turbulence as two independent disturbance factors. Under the situation of the divergent laser propagation

of approximately-point sources, modulation of the transmitted optical beam phase by the atmospheric turbulence can be considered as modulation of the constant phase on the target scattered echo wave. Thus, the unwrapped phase probability density function of the scattered spots transmitted in the atmospheric eddy current can be derived from the following equation:

$$p(\psi)=\int_{-\infty}^{\infty} p(\frac{\psi}{\mu})p(\mu)d\mu \qquad (1)$$

In the equation, $p(\psi/\mu)$ is the probability density function of the speckle phase fluctuation condition in the absence of atmospheric turbulence; p(μ) is the probability density function of the optical wave phase when the atmospheric turbulence are present.

Assume that the compound vibrational amplitude of the echo wave speckle field for target scattering is

$$E=Ae^{i\psi}=A_0e^{i\mu}+R(t)e^{i\varphi(t)}=x+iy \qquad (2)$$

In the equation, x and y are, respectively, the real and the virtual portions of the speckle field E; ψ is the total phase; $A_0e^{i\mu}$ is the constant vibrational amplitude component (not being disturbed) of the light wave; and $R(t)e^{i\varphi}$ is the scattering random component of the field. Since we only can simplify the general elliptical gaussian distribution by coordinate conversion into the distribution product corresponding to interdependent components [6], we consider only in this paper the joint probability density function of the real and the virtual portions

of the following compound vibrational amplitudes [5]

$$p(x,y)=\frac{1}{2\pi\sigma_x\sigma_y}\exp\left[-\frac{1}{2}\left(\frac{\Delta x^2}{\sigma_x^2}+\frac{\Delta y^2}{\sigma_y^2}\right)\right]=p(x)p(y) \qquad (3)$$

Here $\Delta x=x-\langle x\rangle$ is the fluctuation of x; $\langle x\rangle=N\exp(-\sigma^2/2)$ is the mean value of the x component.

$\sigma_x^2=\langle\Delta x^2\rangle=(N/2)[1+\exp(-2\sigma^2)-2\exp(-\sigma^2)]$ is the fluctuation variance of x.

$\sigma_y^2=\langle\Delta y^2\rangle=(N/2)[1-\exp(-2\sigma^2)]$ is the fluctuation variance of y [5]. $\langle\ldots\rangle$ indicates the statistical mean of the system; N is the number of scattering elements of the system; σ is the phase fluctuation standard deviation of the target scattering field.

Eq. (3) indicates the interdependent gaussian distribution of the x and y components of the speckles. This means that Δx and Δy are the dual random circular compound gaussian processes of zero mean value. By introducing the ellipticity parameter

$\rho=2\sigma_x^2/(\sigma_x^2+\sigma_y^2)$, the relationship between the fluctuation intensity $\tilde{I}_x$ and $\tilde{I}_y$ of the two components and the field fluctuation intensity $\tilde{I}=(E-\langle E\rangle)^2$ 与 x、y is

$$\tilde{I}_x=\tilde{I}(1+\rho)/2 \quad , \quad \tilde{I}_y=\tilde{I}(1-\rho)/2 \qquad (4)$$

From probability theory, from the analysis in [6] and the relationship $\tilde{I}=I+I_s-2\sqrt{II_s}\cos(\psi-\mu)$ obtained from Eq. (1) (as shown in Eq. (5)), we can obtain the joint probability density function between the elliptical gaussian process scattering intensity and the total phase ψ when the phase is constrained by

$$p(I,\gamma)=\frac{1}{4\pi\rho\sigma_s^2}\left\{\exp\left[-\frac{I+I_s-2\sqrt{II_s}\cos\gamma}{(1+\rho)\sigma_s^2}\right]-\exp\left[-\frac{I+I_s-2\sqrt{II_s}\cos\gamma}{(1-\rho)\sigma_s^2}\right]\right\} \quad (5)$$

In the equation $\gamma=\psi-\mu$, $I=EE^*$ and $I_s=A_0^2$ 和 $\sigma_s^2=\sigma_x^2+\sigma_y^2$. By using the relationship between the joint probability density and the fringe probability density, we can obtain the phase probability density function

$$p_R(\gamma)=\frac{3\sigma_s^2-\sigma_x^2}{4\sigma_s^2}\left\{\frac{1}{2\pi}\exp\left[\frac{I_s\sin^2\gamma}{(1+\rho)\sigma_s^2}\right]\left[\sqrt{\frac{\pi I_s}{(1+\rho)\sigma_s^2}}\cos\gamma\right.\right.$$
$$\left.+{}_1F_1\left(-\frac{1}{2};\frac{1}{2};-\frac{I_s\cos^2\gamma}{(1+\rho)\sigma_s^2}\right)\right]\Bigg\}-\frac{\sigma_y^2-\sigma_x^2}{4\sigma_s^2}\left\{\frac{1}{2\pi}\exp\left[\frac{I_s\sin^2\gamma}{(1-\rho)\sigma_s^2}\right]\right.$$
$$\left.\times\left[\sqrt{\frac{\pi I_s}{(1-\rho)\sigma_s^2}}\cos\gamma+{}_1F_1\left(-\frac{1}{2};\frac{1}{2};-\frac{I_s\cos^2\gamma}{(1-\rho)\sigma_s^2}\right)\right]\right\} \quad (6)$$

We now consider the weak scattering target when the surface height fluctuation is relatively small ($\sigma_s^2\ll 1$); according to the surface light scattering model of Goodman [7], the scattering field phase ψ is proportional to the boundary fluctuation height $\psi=a+b\eta$. Here a and b are constants. Since by now the phase fluctuation $\gamma=a+b\eta-\mu$ is relatively small, then $\sin\gamma\approx\gamma,\cos\gamma\approx 1$. Because of $\sigma_s^2\ll 1$, then the confluent supergeometric function ${}_1F_1\left(-\frac{1}{2};\frac{1}{2};-x\right)\approx\sqrt{\pi x}$, $x\gg 1$.

From these relationships, we obtain

$$p_R\left(\frac{\gamma}{\mu}\right)=\frac{3\sigma_x^2+\sigma_y^2}{4\sigma_x^2}\left[\frac{1}{\sqrt{\pi(1+\rho)\sigma_\gamma}}\exp\left(-\frac{\gamma^2}{(1+\rho)\sigma_\gamma^2}\right)\right]$$
$$-\frac{\sigma_y^2-\sigma_x^2}{4\sigma_x^2}\left[\frac{1}{\sqrt{\pi(1-\rho)\sigma_\gamma}}\exp\left(-\frac{\gamma^2}{(1-\rho)\sigma_\gamma^2}\right)\right] \qquad (7)$$

In the equation, $\sigma_\gamma^2=\sigma_x^2/I_x$. Actually, Eq. (7) indicates that the x and y directions of the scattering echo waves of a weak scattering target have their phases of the interdependent components satisfying the gaussian distribution. On the other hand, when the target is a smooth plane, the surface fluctuation $\eta=0$. Introduced by reflection, the additional phase ψ is a constant. We assume that this is zero and then we have $\mu=a$. As an approximation, we assume $\sigma_\gamma=\sigma_0$. Then from the standard method [3,4] to convert the density function of the unwrapped phase probability function into the probability density function of the wrapped phase, a summation is made on the probability density function p_ψ in the region of $(-\infty,\infty)$

$$p\left(\frac{\gamma}{\mu}\right)=\sum_{k=-\infty}^{\infty}p_k\left(\frac{\gamma+2k\pi}{\mu}\right)=\frac{3\sigma_x^2+\sigma_y^2}{4\sigma_x^2}\left\{\frac{1}{\sqrt{\pi(1+\rho)\sigma_0}}\sum_{k=-\infty}^{\infty}\exp\left[-\frac{(\gamma+2k\pi)^2}{(1+\rho)\sigma_0^2}\right]\right\}$$
$$-\frac{\sigma_y^2-\sigma_x^2}{4\sigma_x^2}\left\{\frac{1}{\sqrt{\pi(1-\rho)\sigma_0}}\sum_{k=-\infty}^{\infty}\exp\left[-\frac{(\gamma+2k\pi)^2}{(1-\rho)\sigma_0^2}\right]\right\} \qquad (8)$$

By using the simple harmonic decreasing property of $\exp(-x)^2$, mark the equation $\theta=\gamma+2k\pi=\psi+2k\pi-\mu=\Psi-\mu$, $k=0,\pm1,\cdots,(8)$ for Eq. (8)

$$p\left(\frac{\theta}{\mu}\right)=\frac{3\sigma_x^2+\sigma_y^2}{4\sigma_x^2}\left[\frac{1}{\sqrt{\pi(1+\rho)}\ \sigma_0}\exp\left(-\frac{\theta^2}{(1+\rho)\sigma_0^2}\right)\right]$$
$$-\frac{\sigma_y^2-\sigma_x^2}{4\sigma_x^2}\left[\frac{1}{\sqrt{\pi(1-\rho)}\ \sigma_0}\exp\left(-\frac{\theta^2}{(1-\rho)\sigma_0^2}\right)\right],\ -\infty<\theta<\infty \qquad (9)$$

From studying the laser beam in its transmission in atmospheric turbulence, when the divergent laser beam is transmitted and passes through weak turbulence, the instantaneous phase fluctuations satisfies the gaussian distribution

$$p(\mu)=\frac{1}{\sqrt{2\pi}\ \sigma_\mu}\exp\left[-\frac{(\mu-\mu_0)^2}{2\sigma_\mu^2}\right] \qquad (10)$$

In the equation, $\mu_0=\langle\mu\rangle$, $\sigma_\mu^2=b/2A'^2$; b is the random-component variance of the scattering field in the eddy current, and A' is the coherent component of constant vibrational amplitude of the eddy current scattering field. Under certain eddy current conditions, $\sigma_\mu^2=0.78k^2LC_n^2L_0^{5/3}$; L_0 is the exterior dimension of the turbulence; L is the distance from the light source to the receiver; $k=2\pi/\lambda$ is the number of waves; and C_n^2 is the structural constant of atmospheric refractivity. Substitute Eqs. (9) and (10) into Eq. (1), and we can obtain that the unwrapped phase probability density function of the target scattering echo wave in propagation in atmospheric turbulence is

$$p(\Psi)=\frac{3\sigma_x^2+\sigma_y^2}{4\sigma_x^2}\left\{\frac{1}{\sqrt{2\pi[\sigma_\mu^2+(1+\rho)\sigma_0^2/2]}}\exp\left[-\frac{(\Psi-\mu_0)^2}{2[\sigma_\mu^2+(1+\rho)\sigma_0^2/2]}\right]\right\}$$
$$-\frac{\sigma_y^2-\sigma_x^2}{4\sigma_x^2}\left\{\frac{1}{\sqrt{2\pi[\sigma_\mu^2+(1-\rho)\sigma_0^2/2]}}\exp\left[-\frac{(\Psi-\mu_0)^2}{2[\sigma_\mu^2+(1-\rho)\sigma_0^2/2]}\right]\right\} \quad (11)$$

If the scattering echo wave is circularly symmetric gaussian distribution speckle, ρ=1, then Eq. (11) degrades into the results obtained in reference [4].

$$p(\Psi)=\frac{1}{\sqrt{2\pi}\ \sigma_\varphi}\exp\left[-\frac{(\Psi-\mu_0)^2}{2\sigma_\varphi^2}\right] \quad (12)$$

Here $\sigma_\varphi=[\sigma_\mu^2+\sigma_0^2]^{1/2}$.

III. Conclusions

As presented in the paper, the model indicates that when the phase fluctuation of light waves caused by turbulence satisfies the gaussian distribution and the height fluctuation (of the scattering surface) ψ^2 is very small, the phase distribution of the unwrapped speckle and eddy current combination, and the speckle field phase of the target scattering echo waves satisfy the distribution of the same rule. This is because, on the one hand, the echo wave phase of scattering by unsmooth boundary surfaces can be dissolved into the summation of random phase and constant phase satisfying the gaussian distribution. On the other hand, we can neglect the noncircularity of the speckles due to the atmospheric eddy current effect as compared to the effect of boundary surface scattering. Therefore, the constant phase of

the boundary surface scattering echo wave due to the effect of atmospheric turbulence also becomes the variable of the gaussian distribution. Moreover, since the eddy fluctuations and the boundary surface fluctuations are statistically interdependent, we can obtain the above-mentioned conclusions from probability theory. The model also indicates when we know the fluctuation variance of the surface height of the scattering surface, the phase variance of speckles or number of scattering elements of the target, and the phase fluctuation variance introduce by the circularity parameter and turbulence, we can obtain the joint phase probability distribution rule of the unwrapped speckle and eddy current combination. Eq. (11) is still adaptable to phase fluctuation wrapped within $-\pi<\Psi-\mu<\pi$.

The first draft was received on November 3, 1992; the final revised draft was received for publication on January 31, 1993.

REFERENCES

[1] Link DJ, Phillips RL, and Andrews LC. *J Opt Soc Am*, 1987, A 4 (2): 374 ~ 378.
[2] Takai N, Kadomo H, and Asakura T. *Opt Eng*, 1986, **25** (5): 627 ~ 634.
[3] Baraket R. *J Opt Soc Am*, 1987, **A4** (7): 1213 ~ 1219.
[4] Draper DC, Holmes JF, and Peacock J. *Appl Opt*, 1992, **31** (18): 3481 ~ 3487.
[5] Uozumi J and Asakura T. *Opt Quantum Electron*, 1980, **12** (4): 477 ~ 494.
[6] 张逸新, 迟泽英. 科学通报, 1991, **36** (9): 661 ~ 664.
[7] Goodman JW. in Laser Speckle and Related Phenomena (Ed. Dainty JC). Springer-Verlag, Berlin. 1975. 7 ~ 75.

HOLE ARRAY IN WAVEFRONT SENSOR

Jiang Zhiping, Lu Qisheng, Liu Zejin,
and Zhao Yijun

Department of Applied Physics,
National Defense University of
Science and Technology
P.O. Box 1, Handan City, Hebei Province

ABSTRACT The principle of hole array wavefront sensor is described and the phase distribution of a 3.8μm DF high power laser beam has been obtained using this method.

KEY WORDS wavefront sensor, DF laser, hole array.

I. Introduction

Because of errors in machining the cavity lens, as well as thermal deformation caused by laser energy absorbed by the cavity lens, output lens, and output window, and nonhomogeneous flowfield, the result will be phase anomalies in the output laser beam. However, phase anomalies strongly affect focusing performance of laser beams and farfield transmission properties [1]. Phase inspection of lasers is one of the key problems in high-powered laser technology. A 3.2-micrometer laser is outputted by a DF chemical laser device; the wavelength is at the

mid-infrared band. By citing an example of the Hartmann-Shack phase detector [2], there are mainly three difficulties: (1) machining is required to install the tuned infrared sublens array, at high difficulty and high cost. (2) A high resolving-power infrared plane array optoelectronic sensor is required, at high cost. (3) The thermal effect of high power will cause additional phase anomalies.

For these reasons, the article adopts a simple hole array phase sensor and presents its principle and experimental layout as well as the data processing method. The phase distribution of the DF laser is measured directly.

II. Principle and Experimental Layout

The measurement principle is the same as that of Hartmann wavefront sensor [2]. The difference is that the small hole array (referred to below as hole array) is used to replace the sublens array in the Hartmann sensor. As shown in Fig. 1, the

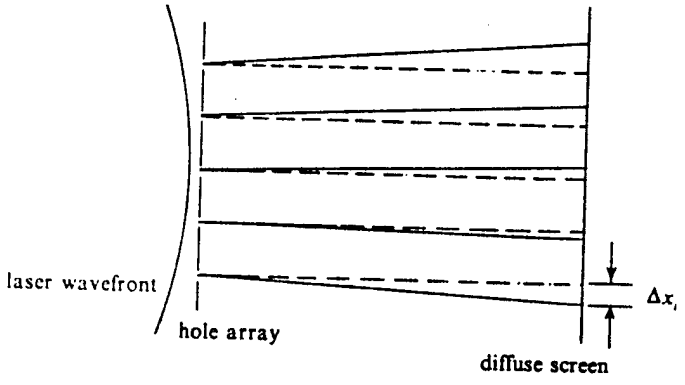

Fig. 1 Principle of hole array wavefront sensor

incident laser beam illuminates the hole array. If the laser beam is a strict plane wave, then the light spot array on the observation screen is the same as that of the whole array (dotted lines). When the laser phase is not planar, since the direction of propagation of light in very small holes is perpendicular to the phase plane at the site, the light passing through these small holes will propagate along solid lines. On the observation screen, there will be a translation of the light spot array position relative to the planar wave. Assume that the translations corresponding to the i-th hole in the x and y directions are, respectively, Δx_i, Δy_i. Moreover, it is assumed that the distance between the hole array and the observation screen is f, then the inclination rate g_{x_i} and g_{y_i} of the wavefront of the i-th hole are:

$$g_{x_i} = \frac{\Delta x_i}{f} \quad , \quad g_{y_i} = \frac{\Delta y_i}{f}$$

therefore, by just measuring Δx_i and Δy_i, g_{x_i} and g_{y_i} can be derived. Thus, a certain algorithm can be used to locate the phase plane of the laser at the hole array.

In practical work, since there can be two work aspects with different conditions: (1) for infrared light with visible light and wavelength less than 1.1micrometers, a silicon CCD plane array optoelectronic sensor can be used as the optoelectronic conversion apparatus (refer to Fig. 2). The silicon CCD camera transforms the light spot arrays on the diffuse reflection screen into electric signals, which are converted to digital signals by the image plate, then to be inputted into a microcomputer for

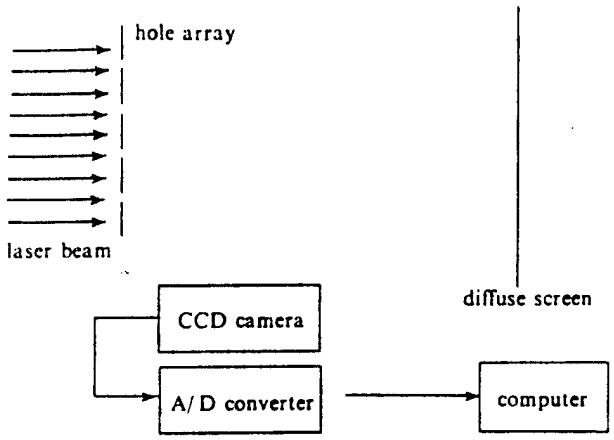

Fig.2 Case of visible or infrared laser beam

processing. (2) For a DF 3.8micrometer laser or a 10.6micrometer CO_2, a method similar to (1) can be used when there is a thermal imaging instrument with corresponding waveband. Otherwise, the observation screen in Fig. 1 can be changed into an organic glass plate. When the laser power is sufficiently high, the laser beam passing through the hole array will burn small holes on the organic glass plate or will leave visible molten tracks. The burn tracks on the organic glass are inputted into the computer with a scanner. Method (2) is used in this article.

III. Experimental Results

We take into account the spatial resolving power at diffraction, and the hole spacing of the hole array is 4.0mm and the small hole diameter is 1.5mm. To avoid the laser beam outside the hole being reflected into the laser device, the small

hole axial line and the normal line to the hole array plate are processed into an angle of about 15^{0}. Fig. 3 shows the burn track recorded on the organic glass.

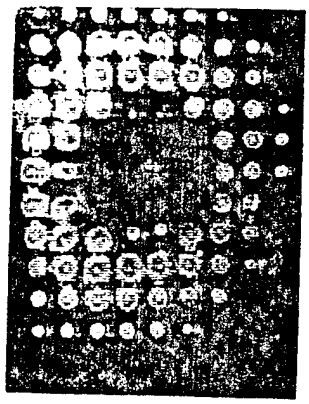

Fig. 3 Burn hole on lucity

The spacing (between the organic glass plate and the hole array) f=50cm. The ratio between the figure and the object size is 1:1. The figure is plotted with an HP Scanjet Plus scanner to input the information on the organic glass plate into the computer and then with laser printer output. The resolving power of the scanning instrument is 300 dots per inch; in other words, the spacing between the lines is 0.0847mm. The light spot position on the organic glass plate is given by the center of the burn track shape. The wavefront structure adopts the Southwell regional method [3]. See Fig. 4 for phase distribution.

IV. Conclusions

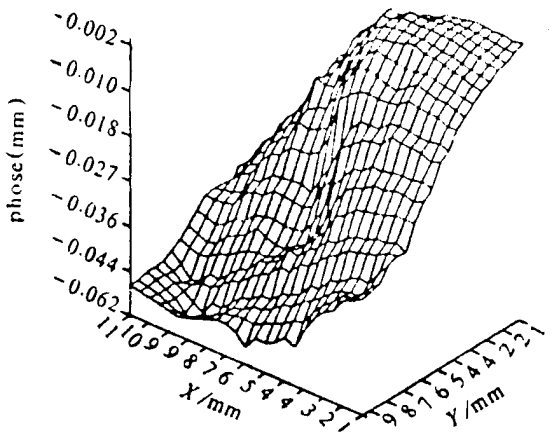

Fig. 4 Wavefront of DF laser beam after reconstruction

By using the hole array method, the phase plane of the DF laser is directly measured. Compared with the conventional Hartmann sensor, the hole array method has the following advantages: (1) the equipment is quite simple. It only requires a metal plate and an organic glass plate to be drilled with a small hole array, without requiring precise adjustment. The cost is very low. (2) The hole array can be used in visible light or in infrared light. To a certain extent the difficulties of phase measurement of infrared lasers are solved. (3) High-powered lasers can be directly measured without deterioration. (4) There is higher spatial resolving power. (5) In the optical path, no additional optical elements are required, therefore there is no additional phase anomaly. However, there are some problems remaining to be improved: one is the precise measurement of the light spot position. Secondly, the time dependent variation difficulties are greater for measuring the wavefront by using the burn track method with an organic glass plate. Equipment similar

to that of Fig. 2 can replace the organic glass burn hole with a thermal instrument. The authors are developing studies in this area.

The first draft of the paper was received on January 31, 1993. The final revised draft was received on April 1, 1993.

REFERENCES

[1] Claude AK. Wavefront distortions in power optics. *SPIE*, 1981, 293.

[2] Robert KT. Principle of Adaptiv Optics. Academic Press, Inc. 1991.

[3] 周仁忠，阎志祥. 自适应光学(下册). 北京工业学院出版社，1983.

NEW ADVANCES IN UNSTABLE OPTICAL RESONATORS

Zhou Dazheng

Dalian Institute of Chemical Physics
Chinese Academy of Sciences
P.O. Box 110, Dalian 116023

ABSTRACT The recently appeared several nevel optical unstable resonators are reviewed. Their characteristics and development are analysed.

KEY WORDS novel optical unstable resonators.

I. Introduction

For large-energy high-powered laser devices, the most important matter is dealing with the contradiction between laser output energy and light beam quality. The optical resonator in practice follows tradeoff in selective principles between energy output and light beam quality to achieve large-mode with prerequisite light beam quality of indicators to obtain near-diffraction limit Gaussian beam operating at TEM_{00} mode in the small nearby region of the optical-axis center for the classical stabilized cavity in intermediate and low-powered laser devices. However, for large mode size, in addition to prolonging the cavity length but also using an in-cavity optical beam-widening

element, this will induce phase anomalies due to image difference of beam expansion elements and optical element easily damaged by the laser in the cavity.

However, for laser devices with large Fennell number it is not practical to obtain a large volume output of the fundamental mode. For the ring-shaped outputted concave and convex stabilization cavity, if the parameter g can be strictly controlled within the criterion range of the stabilization region, theoretically speaking a greater-size fundamental-mode output can also be obtained. Since the design conditions are too strict, only when $\Delta=L+R_{convex}-R_{concave}$ approaches zero, and $g_1 g_2 \dashrightarrow 1$, can the above-mentioned output be obtained at the fringe of the stabilization region. Therefore, the machining precision and alignment adjustment of the resonator are especially difficult. Later, such cavities were replaced with conventional confocal unstable cavities.

The conventional confocal unstable cavity can be used to obtain large-mode volume; however, the ring-shaped output beam is quite sensitive to maladjustment of the mirror and anomalies in the mirror surface, thus causing inhomogeneity of the laser patterns in the near-field of the ring-shaped beam. It is very easy to damage the window of a high-powered laser device. However, the far-field light beam patterns still unavoidably produce many diffraction rings affecting light beam quality. On account of this, the divergence of the 10,000-W class CW CO_2 laser device by using the conventional unstable cavity is still

unable to be attained within several times the diffraction limit. This ring-shaped diffraction output cavity has another flaw. Within the range of the diffraction bandwidth (λ/Θ) at the fringe of the mirror (Θ is the diffraction output angle of the light beam at the fringe of the mirror), since the thermal deformation of the lens or due to processing and installation, the angle Θ is sufficiently large, some light beams outputted with oscillation diffraction of the laser in the cavity will return to the center zone of the optical axis in the cavity along the route of its coming, to excite the new low-valency transverse mode period, inducing a complicated mode structure. This situation will be more serious with an increase in laser power, in particular, for lower-gain laser devices adopting the low amplifying-rate design to upgrade the light beam quality and eliminate the side lobe effect, as well as to eliminate the effect on complex mode structure in the cavity due to the hard edges of the lens. Thus, the various low-order modes separate and achieve the complete fundamental mode operation require the development of novel unstable cavity with large-mode volume.

In recent years, on several occasions abroad proposals for unstable cavity methods of large mode volume to greatly upgrade the light beam quality of high-powered lasers were proposed. This article will detail and discuss these novel unstable cavities with application prospects given.

II. Several Novel Unstable Cavities

2.1. Radial variable-reflectivity mode unstable resonator (RVRMUR)

This cavity is also called the unstable cavity with a Gaussian reflectivity output coupler (GRC). This cavity adopts the step-by-step output approach of transmission. Therefore, the effect on the fundamental mode operation by complex mode structure in the cavity due to the hard edges of the conventional unstable cavity can be eliminated. In the method, by adjusting the reflectivity at the mirror surface, the distribution of mirror surface reflectivity is of a Gaussian function. In 1970, H. Zucker et al. were the first to propose this concept [1]. However, since the output mirror technique has not been qualified, this technique was not emphasized in the academic field. Only several researchers conducting experiments confirm this theory on laser devices with relatively low power and relatively small cross-sectional area [2-5].

In 1985, P. Lacigne et al. in Canada coated the high reflectivity medium mode varying with the mirror diameter onto the substrate with an antireflection treatment. In addition, denaturation with transmission of nonreflected light to remedy the unstable cavity that the Gaussian reflectivity mirror is used as the output coupler. Then this technique was applied in high-power CO_2 laser devices. By applying the output mirror with the Gaussian reflecting surface, the harmful effect of mirror edge diffraction in conventional unstable cavity can be reduced. In addition the second diffraction ring in the distribution of far-

field intensity is eliminated, thus, upgrading the directivity and brightness of the light beam [7]. In 1988, S. deSilvestri et al. proposed a super-Gaussian-reflectivity mirror [8]. The fundamental-mode volume of the unstable cavity with this output mirror is greater than the former one, and the laser output efficiency is also higher. In a high-Fennell-number resonator, good light beam quality can also be obtained although from the super-Gaussian reflective type surface equation, we obtain

$$R_r = R_0 \exp[-2(\frac{r}{W_m})^n] \quad (n>2) \qquad (1)$$

In the equation, R_0 is the reflectivity at the center of the output coupler; r is the radius of the mirror; and W_m is the radius at the GRC reflectivity curve 1/e. We can see that, with increase in n, the super-Gaussian indicator, the diametral direction reflectivity type surface curves gradually have the flat-topped phenomenon, which is disadvantageous to mode selection. However, even if 9 is selected for m, in the CO_2 and YAG laser devices, experiments proved that a super-Gaussian mirror can still produce beams with near-diffraction limit, and can output a higher energy over the classic unstable cavity.

This cavity is composed of a piece of concave surface 100%-reflective mirror and a piece of output coupling mirror with variable reflectivity output at the diametral direction of the convex surface. In this cavity type, light beam waist in the cavity is determined by the following equation:

$$W_h = \sqrt{M^2 - 1}\, W_m \qquad (2)$$

In the equation, M is the amplifying rate of the optical cavity; W_m is the radius of the GRC reflectivity curve at 1/e.

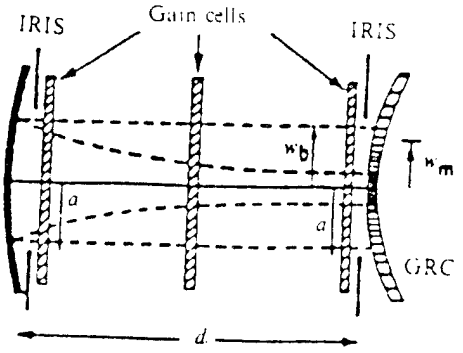

Fig. 1 Unstable resonator with gaussian reflectivity mirror

By varying the mirror waist W_b and the optical cavity amplifying rate M, and by using Eq. (1), we can obtain any Gaussian beams. The distribution of the near-field optical-beam intensity after using this cavity type can be expressed by using the difference of two Gaussian functions:

$$I_{n,0} = I_{n,0}\exp\{-\frac{r^2}{W_b^2}\}[1 - R_0\exp\{-\frac{r^2}{W_m^2}\}] \qquad (3)$$

In the equation, r is the diametral distance from the optical axis, and $I_{n,0}$ is the light intensity at the GRC center optical axis.

If the center reflectivity $R_0 > (1 + \frac{W_b^2}{W_m^2})^{-1}$ sinking at the center will appear in the near-field distribution (Fig. 2). The dotted lines in the figure indicate the unstable cavity, while solid lines indicate the unstable cavity with a phase-unifying coupler. When the transmission beam is straightened with the GRC

and the far-field brightness, when $R_0 \approx 1$, is the highest, when $W_b / W_m \geq 1$, the far-field intensity can be approximately determined by the following formula

$$I_{f,\theta} = I_{f,0}\left[\exp\{-\frac{\theta^2}{\theta_0^2}\} - \frac{R_0}{2(1+\frac{W_b^2}{W_m^2})}\exp\left\{-\frac{\theta^2}{(1+\frac{2W_b^2}{W_m^2})\theta_0^2}\right\}\right]^2 \qquad (4)$$

In the equation, $\theta_0 (= \lambda / 2\pi W_b)$ is the divergent half-angle at the maximum intensity 1/e of the Gaussian beam in the cavity; $I_{f,0}$ is the light intensity at the center optical axis of the far field.

From the far-field intensity distribution diagram, we can see that the second diffraction ring of the far-field light beam has been severed (Fig. 3). Another advantage of the unstable cavity of this diametral variable-reflectivity mirror is its nonrestraint by the gain cross-section. Although the mismatching of the cavity adjustment will lower the output energy of the light beam, but it does not affect the output of the far-field solid-core Gaussian type surface.

Fig. 4 shows the fundamental design of the GRC reflected-output mirror. The output mirror is composed mainly of multilayer high-refractivity medium film with a certain shape chemically deposited on the anti-reflection medium substrate. Some of the unreflected light passes through the anti-reflecting substrate. Along with the diametral variation, the thickness of the medium film surface can be derived from the theory of multiple light-beam interference of the thin film of the medium.

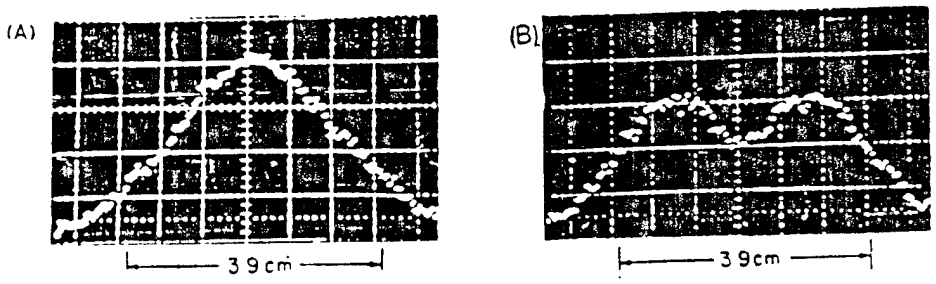

Fig. 2 (A) Intracavity and (B) near-field intensity distributions of the beam produced in a resonator ($M=2$) with a GRC ($W_0=1.2$cm, $R_0=0.7$)

$$\delta_r = \frac{\lambda_0}{4\pi n_2} \cos^{-1}\left\{ \frac{1}{2r_{12}r_{eq}} \left[\frac{(1-r_{12}^2)(1-r_{eq}^2)}{1-R_r} - r_{12}^2 r_{eq} - 1 \right] \right\} \qquad (5)$$

In the equation R_r is the diametral reflectivity; λ_0 is the designed wavelength in vacuo; n_2 is the reflectivity of the medium film; r_{12} is the reflectivity of the surface amplitude in the medium between 1 and 2; r_{eq} is the amplitude reflectivity at the inner surface of the antireflecting film substrate.

Generally in abroad, the film coating of such mirrors applies the chemical vapor deposition (CVD) method. In other words, this is the application of a gaseous substance to have a chemical reaction at the solid surface in the process of forming a solid deposit. Therefore, the affinity between the formed film and the substrate is better than the physical vapor deposition method (PVD). The CVD process can take place at constant pressure, and also at low pressure. Since at low pressure the diffusion rate of a gaseous reflecting substance is greater than that at constant pressure, this has a good function on the

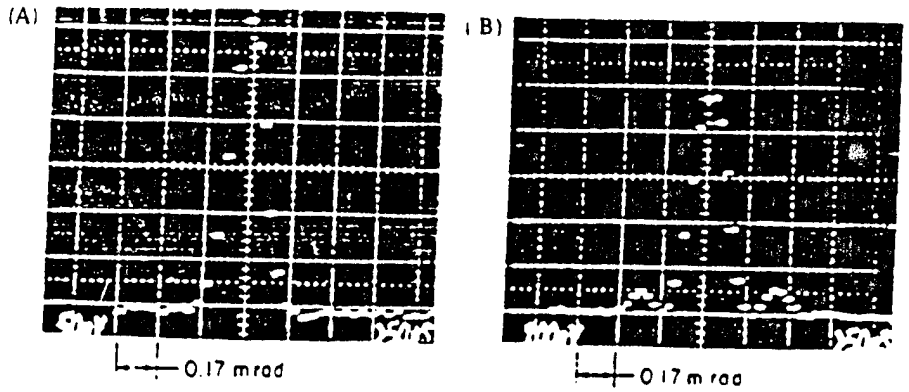

Fig. 3 Far-field intensity distribution of the beam coupled out of a resonator ($M=2$); (A) through a 12.5cm-diameter GRC ($2W_0=2.4$cm) and (B) around a 2.5cm-diameter hard-edged mirror

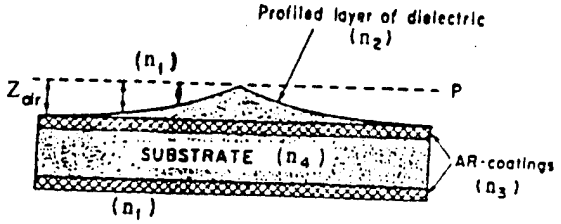

Fig. 4 Configuration of the complementary Gaussian reflectivity mirror

diffusion, adherence, reaction, and growth of film substance between the reactive substance and the matrix. Therefore, there is obvious improvement in the quality of the film layer. Thus, in recent years, the low-pressure method was applied in CVD. Generally, using CVD in making thin films is divided into four main stages: (1) surface diffusion of the reactive gas toward the matrix; (2) adherence of the reaction gas onto the surface of the

matrix; (3) chemical reactions occur at the matrix surface; (4) on the surface of the matrix, the gaseous by-products produced are detached from the surface and are pumped out and discharged by the vacuum pump, so a firm reactive substance remains on the substrate surface. Previously, the CVD had not been extensively promoted. The main reason was the higher deposition temperature. In recent years, many specialists conducted studies on lowering the thin film deposition temperature and explored new reaction excitation methods. Good progress was obtained. The more successful of these methods is the molecular beam extension technique, combining the plasma excitation chemical vapor deposition method (FECVD), and the laser induced-chemical vapor deposition method. Therefore, in present-day international practice the CVD method has replaced the PVD method in making high-energy and high-powered cavity mirrors. In the process of CVD preparing of the diametral variable-reflectivity cavity mirror, the key technique is that of (1) for the development and determination of the dynamic parameters of the chemical gaseous source in the components of the coated-film system and the reaction process (the concentration, reaction temperature, and pressure of the chemical reactant). (2) Study and determine the shape parameters of the shielding apparatus in the CVD chamber, and the relative position of the deposited substrate.

From the foregoing, by using the diametral variable-reflectivity unstable cavity coupled with the GRC, the side lobe

pattern in the far-field intensity distribution can be eliminated in order to upgrade the light beam directivity and brightness. This is attractive for the low-gain and low amplifying-rate resonators with the second diffraction ring occupying the higher proportion. The machining of this type of cavity mirror is complex. Currently, there are only a few countries in the world that have developed successfully. In particular, there have been no development reports on the variable-reflectivity mirror with X-Y axial symmetry with rectangular output light beam and light cavity. In the author's view, although this film coating machine is more complicated in structure and processing technique, yet this is a new approach. Its success will mark the occasion of a high degree of unification of light beam quality and laser output efficiency of the intermediate and low-gain transverse-flow laser devices.

2.2. Phase-Unifying Output Coupler with Unstable Resonator (PUCUR)

In 1988, S. Yagi et al. in Japan were the first to publish a paper on an unstable resonator with phase-unifying output coupler. This is also called an unstable resonator with diametral graduated variable-reflectivity mirror [9]. Such cavity has partial reflection from its center, composed of output-coupled mirror and an all-concave reflecting mirror with anti-reflectivity at the fringe (Fig. 5). The film-coating processing method for this output mirror is actually a variety and a simplification of the diametral variable super-Gaussian-

reflectivity output mirror. Its selective capability in the

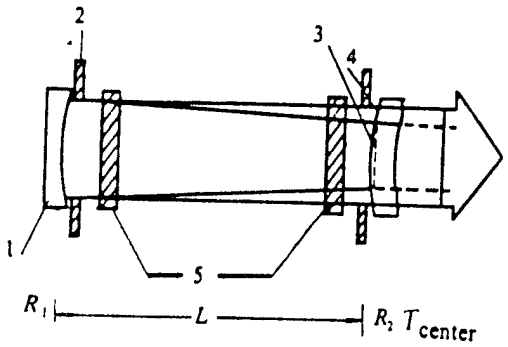

Fig. 5 Unstable resonator with phase-unifying coupler

transverse mode is less than that of the unstable resonator of the super-Gaussian-reflectivity mirror with smaller m. However, its mode volume utilization is close to that of the resonator with a greater super-Gaussian reflectivity mirror. So such unstable resonator is more suitable to the CO_2 laser device with longer wavelength and intermediate gain. Since this also adopts the output approach with transmittance or mainly with transmittance, therefore this does not have the harmful effect of hard-edge diffraction of the conventional mirror with unstable resonator. Such unstable resonator can be used to induce the phase-unified far-field light beam with large volume of desirable pattern.

On the initial field distribution of the diametral light beam, on the surface of this type of resonator mirror, let us

assume that the pseudorandom distribution of the field vibration amplitude and phase on this mirror surface is $U(r_1)$, with Fennell

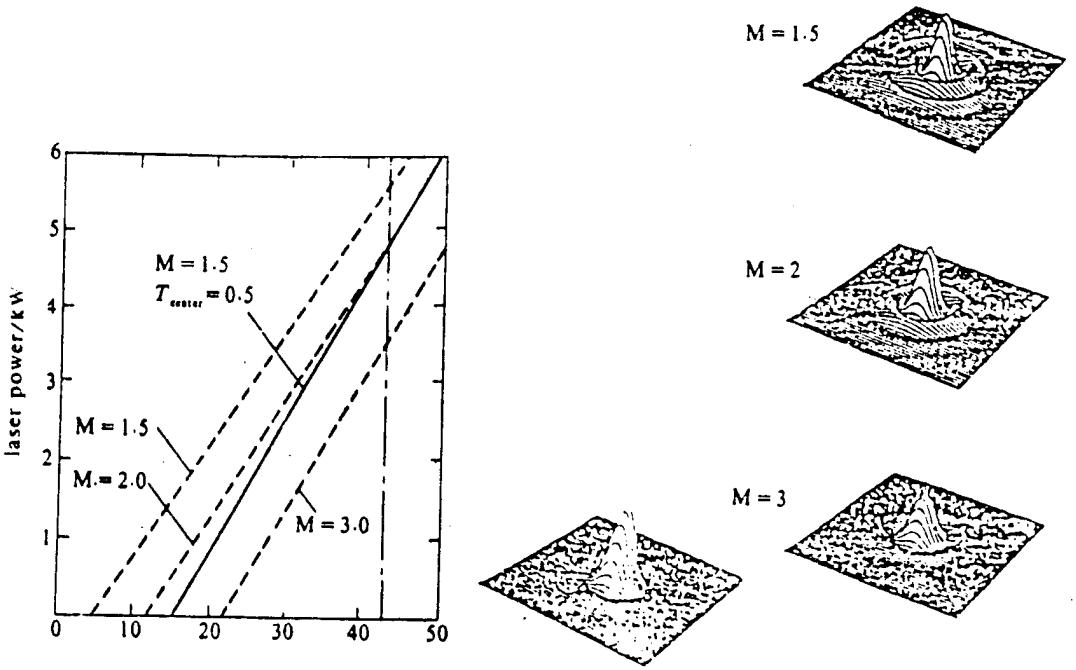

Fig. 6 Comparison of laser power and far－field beam pattern
(a) laser power vs discharge power, and far－field patten of (b) the novel resonator, and (c) Conventional unstable resonator at a discharge power of 43kW

integration, the field distribution $U(r_2)$ on the mirror of the opposite surface can be determined. After the light beam makes several round trips, the field distribution in the resonator reaches the saturation state, then

$$U(r_2) = 2\pi \iint_{|r_1| < a_1} K(r_1, r_2)\, U(r_1)\, r_1 dr_1 \tag{6}$$

but

$$K(r_1, r_2) = \frac{\exp\{ik\sqrt{(r_2 - r_1)^2 + L^2} + \sqrt{[g_1(r_1) + g_2(r_2)]L}}{i\lambda\sqrt{(r_2 - r_1)^2 + L^2}} \tag{7}$$

In the equation r_1 and r_2 are the diametral distances of the mirror; L is the resonator length; $k=\lambda/2\Pi$, λ is the wavelength; a_1 is the radius of the reflected disk; and functions $g_1(r)$ and $g_2(r)$ are the gains of the oscillation amplitude in front of each mirror.

Assume that the saturation gain is given by the formula:

$$g=\frac{g_0}{[1+(I_a+I_b)/I_s]} \tag{8}$$

In the equation, g_0 is the small-signal gain of the medium; I_a and I_b are the local field intensities of the plane wave propagation; I_s is the saturation strength.

The complex oscillation amplitude function relates to the electric field

$$E(r)=\mathrm{Re}\,U(r)\exp(-iW_0t) \tag{9}$$

In the equation, $W_0=2\Pi c/\lambda a$, c is the speed of light.

In the resonator, intensity I(r) and phase P(r) can be calculated from the following equations:

$$I(r)=|U(r)|^2 \tag{10}$$

$$P(r)=\arctan\{\frac{\mathrm{Im}\,U(r)}{\mathrm{Re}\,U(r)}\} \tag{11}$$

Fig. 5 shows the light beam patterns of the near- and far-fields after the CO_2 laser adopts such kind of resonator. By making a comparative experiment, it was discovered that by using this new unstable resonator, its power output is slightly less than that of a conventional unstable resonator. In the former,

the power output level of M=1.5 approaches that of a conventional unstable resonator designed on the basis of M=2. However, the high focusing beam of the solid pattern generated by this cavity (M=1.5) is better than that of a conventional resonator (M=3) (fig. 6) [10]. S. Yagi et al. of the Mitsubishi Electric Corporation in Japan obtained linearly-polarized light with a divergence angle of 0.6mrad with a 5kW CO_2 coronal discharge transverse-flow laser device. Based on the output aperture of 45mm, calculation yielded the diffraction limit.

2.3. Self-filtering Unstable Resonator (SFUR)

By adopting the high-amplifying-rate design for conventional high-gain, high-power laser device, its conventional unstable resonator can produce better light beam quality. However, this is very difficult to adopt the high-quality laser beam by using the same approach for the high-power short-pulse excimer laser device. The reason is that the gain buildup time for such laser device is considerably shorter than the mode buildup time, therefore it is unable to reach the diffraction limit.

In 1984, P. G. Cobbi et al. in Italy [11] were the first to realize a negative-branch unstable resonator of the self-filtering unstable type (SFUR) (Fig. 7). Such resonator includes a field-limiting aperture (LA). The small-hole radius (of the aperture) $a = \sqrt{0.61 f_2 \lambda}$. The resonator is situated at the confocal point with focal lengths f_1 and f_2 of the confocal points of two concave-surface reflecting mirror M_1 and M_2. When

the plane wave impinges on LA and reflects back from the mirror

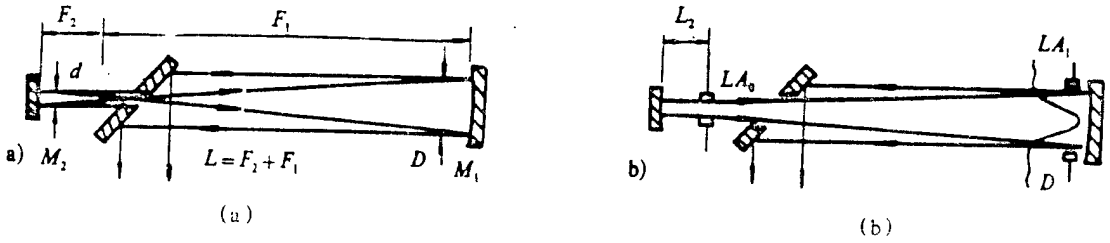

Fig. 7 Schemes of unstable resonators
(a) self-imaging unstable resonator; (b) modified form of self-filtering unstable resonator

M_2 with smaller radius of curvature, only the Airy disk is allowed to be propagated outside of the hole, and makes a round-trip inside the resonator with amplifying rate $M=-f_1/f_2$. This scheme is especially suitable to high-gain laser devices such that the stable low-order mode can be quickly established in the resonator. However, when SFUR is used for a short-pulse excimer laser device, generally the mode volume is very small. To let it fill the entire active volume cross-section in order to obtain high-level energy, recently P. D. Lazzaro [12] proposed a generalized self-filtering unstable resonator (Fig. 8).

To obtain the SFUR property with the same feature, it is required to introduce two conditions: (1) self-imaging condition; this is the relationship between l_1 and l_2, on the one hand, and f_2, on the other, in order to satisfy the requirement that the mirror image of the needle hole corresponds to the surface of the needle hole itself after one round trip between the mirror

surfaces. (2) To interrupt the oscillation of the TEM_{00}

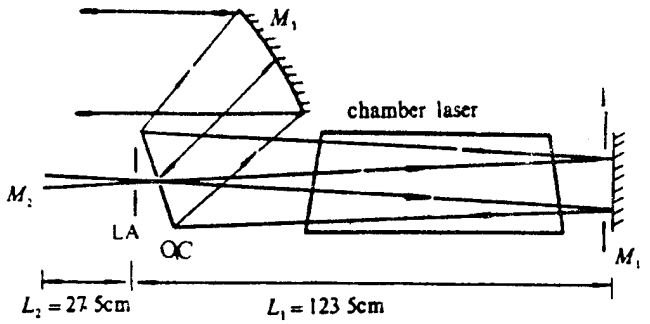

Fig. 8 Schematic diagram of the GSFUR
M_1 : aluminized flat mirror; M_2 : aluminized concave mirror of focal length f_2;
OC : output coupler ; LA : field – limiting aperture ; M_3 : aluminized collimating mirror of focal length f_3 ; d : distance of M_3 from OC

intrinsic mode of the shorter portion of the light path separated by the LA in the optical cavity, it is required to select the needle hole radius.

If
$$L_1 g_1 (2g_2 - 1) = -L_2 g_2 (2g_1 - 1) \qquad (12)$$

The condition of (1) can satisfy the requirement that L_1 and L_2 in the equation are, respectively, the distances of M_1 and M_2 from the aperture LA.

$$g_1 = 1 - \frac{L_1}{2f_1} \quad ; \quad g_2 = 1 - \frac{L_2}{2f_2} \qquad (13)$$

For the planar mirror M_1, $g_1=1$. From Eq. (12), we can obtain

$$L_2 = f_2 (1 + \frac{f_2}{2L_1}) \qquad (14)$$

To interrupt the oscillation of the intrinsic mode oscillation

(TEM_{00}) in the L_2 region, the radius of the LA aperture should be

$$a=\sqrt{g_2 L_2 \lambda} \qquad (15)$$

In this cavity, the amplifying rate is

$$M=-\frac{L_1}{g_2 L_2} \qquad (16)$$

From the above equation, we can see that the amplifying rate can be varied by changing the distance to L_1. From Fig. 8, we can see that there is some bending of the wave array surface of modes in the light cavity. To obtain the output light beam near the needle-hole screen, the alignment output should require the reflective mirror M_1, with focal length as

$$f_3=d-\frac{2g_2 L_2}{2g_2-1} \qquad (17)$$

In the equation, d is the distance between aperture LA and M_3.

For this self-filtering unstable resonator in the broad sense, to obtain large mode volume, the amplifying rate should be very large (generally, M is greater than or equal to 10). In recent years, such unstable resonators have been successfully operating in the Nd:YAG lasers and the TEA CO_2 excimer lasers. In particular, the unique feature can be better exploited in the high-gain, high-power, short-pulse excimer device that the stable low-order mode is unable to be established quickly. After the ultraviolet pre-ionized XeCl laser device adopts the plane and concave self-filtering unstable resonator, the diffraction-limit Gaussian laser beam has been obtained for 11ns short-pulse

lasers, with brightness at 4.8×10^{13} $Wcm^{-2}sr^{-1}$. If wave chopping or other technique of complex pulse width is adopted to increase the brightness of the laser apparatus by two orders of magnitude, this is very possible to be used in research on ICF. However, it is required to have high magnifying power for this type of cavity, and this is not suitable for low-gain, high-power lasers. This is also of the negative-branch unstable resonator and needle-hole surface plate in the cavity that is very easily damaged. Due to the cavity length being long in the experiments, requirements on straightening of the cavity are also quite high.

Table 1 Advances in unstable resonators

No	resonator type	laser set	outpower	$\theta_{f.e}$
1	GRC VRUR	CW CO_2	300W	0.35mrad
2	GRC VRUR	pulse YAG	385mJ, 0.5 ~ 5Hz	0.26 ~ 0.69mrad
3	PUCUR	CW CO_2	5kW	0.6mrad φ45
4	GFSUR	short-pulse XeCl	3.5mJ 11ns $4.8 \times 10^{13} Wcm^{-2}sr^{-1}$	0.26mrad

III. Conclusions

The three above-mentioned new models of unstable resonators have good prospects in the high-energy (or high-power) large-mode-volume unstable resonators. Table 1 shows the development level obtained at present.

In Table 1, the GRC VRUR is suitable to high-powered lasers

of intermediate and low gain. The advantage can be more exhibited in the low-gain laser device. PUCUR is suitable to the intermediate-gain laser devices. SFUR and GSFUR are suitable for high-gain laser devices. Other than the three above-mentioned new unstable resonators, recently there has been the beam-rotating laser device and the diffraction filtering unstable resonators, represented by UR90. It is noteworthy that vigorous research is also underway in the United States.

The first draft was received on December 21, 1992; the final revised draft was received for publication on April 5, 1993.

REFERENCES

[1] Zucker H. *Bell Syst Tech, J*, 1970, **49**:2349.
[2] Yariv A and Yeh P. *Opti Commun*, 1975, **13**:370.
[3] Casperson LW and Lunnam SD. *Appl Opti*, 1975, **14**:1139.
[4] Mccarthy N and Lavigne P. *Appl Opti*, 1983, **22**:2704.
[5] Mccarthy N and Lavigne P. *Appl Opti*, 1984, **23**:3845.
[6] Lavigne P et al. *Appl Opti*, 1985, **24**:2581.
[7] Mccarthy N and Lavigne P. *Opti Lett*, 1985, **10**(11):553.
[8] Silvestri S de. *IEEE J Quant Electro*, 1988, **24**(6):1172.

DISTRIBUTION LIST

DISTRIBUTION DIRECT TO RECIPIENT

ORGANIZATION	MICROFICHE
B085 DIA/RTS-2FI	1
C509 BALL0C509 BALLISTIC RES LAB	1
C510 R&T LABS/AVEADCOM	1
C513 ARRADCOM	1
C535 AVRADCOM/TSARCOM	1
C539 TRASANA	1
Q592 FSTC	4
Q619 MSIC REDSTONE	1
Q008 NTIC	1
Q043 AFMIC-IS	1
E404 AEDC/DOF	1
E410 AFDTC/IN	1
E429 SD/IND	1
P005 DOE/ISA/DDI	1
1051 AFIT/LDE	1
PO90 NSA/CDB	1

Microfiche Nbr: FTD95C000758
NAIC-ID(RS)T-0512-95